

See discussions, stats, and author profiles for this publication at: <https://www.researchgate.net/publication/224895430>

Ultrafast Shock Compression and Shock-Induced Decomposition of 1,3,5-Triamino-2,4,6-trinitrobenzene Subjected to a Subnanosecond-Duration Shock: An Analysis of Decomposition Produc...

ARTICLE in THE JOURNAL OF PHYSICAL CHEMISTRY A · MAY 2012

Impact Factor: 2.69 · DOI: 10.1021/jp301771y · Source: PubMed

CITATIONS

5

READS

37

5 AUTHORS, INCLUDING:



[Joseph M Zaug](#)

Lawrence Livermore National Laboratory

120 PUBLICATIONS 1,186 CITATIONS

SEE PROFILE



[A. J. Nelson](#)

Lawrence Livermore National Laboratory

250 PUBLICATIONS 2,853 CITATIONS

SEE PROFILE



[Michael R. Armstrong](#)

Lawrence Livermore National Laboratory

71 PUBLICATIONS 664 CITATIONS

SEE PROFILE



[M. Riad Manaa](#)

Lawrence Livermore National Laboratory

90 PUBLICATIONS 1,528 CITATIONS

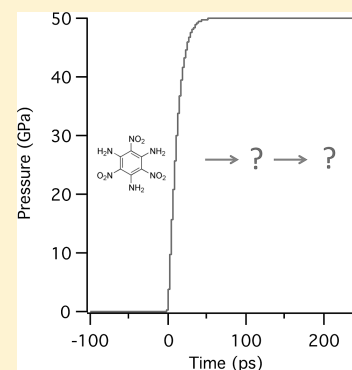
SEE PROFILE

Ultrafast Shock Compression and Shock-Induced Decomposition of 1,3,5-Triamino-2,4,6-trinitrobenzene Subjected to a Subnanosecond-Duration Shock: An Analysis of Decomposition Products

Jeffrey A. Carter,* Joseph M. Zaug, A. J. Nelson, Michael R. Armstrong, and M. Riad Manaa

Chemical Science Directorate, Lawrence Livermore National Laboratory, P.O. Box 808 L-350, Livermore, California 94550, United States

ABSTRACT: Shock compression studies of pressed and confined ultrafine 1,3,5-triamino-2,4,6-trinitrobenzene (TATB) powder were conducted using ultrashort ~ 300 ps, ~ 50 GPa shock waves. The recovered decomposition products were characterized using X-ray photoelectron spectroscopy, infrared spectroscopy, and Raman spectroscopy. A substantial amount of shock-related chemistry was observed. Approximately 75% of the nitrogen atoms were liberated as gas-phase species, along with $\sim 33\%$ of the oxygen atoms, as a result of the applied shock. Furthermore, we observe C 1s binding energies suggesting the formation of sp^3 hybridized amorphous carbon. For comparison, a carbon nitride material was also prepared and characterized by thermally pyrolyzing TATB. The shock-compressed TATB and the thermally pyrolyzed TATB are qualitatively different, suggesting that, carbon nitrides, a possible indicator of nitrogen-rich heterocycles precursors, are not a major product class for strongly overdriven shock conditions. These experimental conditions were, however, not detonation conditions, and the possible formation of nitrogen-rich heterocycles in actual detonations still exists.



1. INTRODUCTION

Carbon-rich explosives, such as 1,3,5-triamino-2,4,6-trinitrobenzene (TATB), tend to have considerably slower reaction times and thus necessarily longer reaction zones compared to other organic energetic materials.¹ The origin of this phenomenon is generally prescribed to diffusion-limited growth of larger solid carbon soot particles from smaller carbon clusters.^{2–5} The starting size of these carbon clusters, which are thought to condense out from liquid carbon, is not well-known. From a modeling perspective, the starting size of these clusters affects the diffusion-limited growth of solid carbon and thus the corresponding rate of energy release. The current practice for thermochemical codes is to use parameters that best match experimental results.⁶

An alternative mechanism was recently proposed that could account for the delayed energy release for the shock-induced decomposition reaction of TATB and possibly other carbon-rich energetic materials. Manaa et al. used quantum-based atomistic simulations of shock-compressed TATB and showed that high concentrations of nitrogen-rich heterocyclic species are present on the subnanosecond time scale of shock-induced decomposition.⁷ These heterocyclic species could act as a nitrogen sink, retarding the release of chemical energy that accompanies the formation of N_2 and solid carbon. Their simulation results for an overdriven shock velocity of 9 km/s showed the initial decomposition product H_2O within approximately 20 ps after shock compression, while the onset of N_2 and CO_2 formation is delayed by approximately 100 ps and concentration of these species continued to increase over the duration of the simulation window. The impeded formation

of N_2 and CO_2 was a consequence of the formation of nitrogen-rich heterocycles, which contained a majority of the available nitrogen and carbon for simulation times up to 400 ps. If this mechanism is correct, then new chemistry will need to be included in thermochemical codes.

Observation of carbon nitrides in shock-induced decomposition reactions would provide supporting evidence for the existence of the proposed nitrogen-rich heterocycles. Thermodynamic arguments have suggested that the formation of carbon nitride materials during detonations is feasible from an energetic standpoint.^{8,9} In fact, the minimum pressures and temperatures (60 GPa, 2000 K) obtained from the overdriven simulations of Manaa et al., along with the theoretical, albeit extrapolated, phase diagram reported by Odintsov et al., suggest that β - C_3N_4 is a thermodynamically stable species.⁸ The time scale, however, for carbon nitride formation is unknown under these conditions. β - C_3N_4 was chosen here as a representative carbon nitride material, we have no way of predicting an actual stoichiometric ratio for these possible products. In fact, several different crystalline phases of carbon nitrides have been observed from shock-compression events of nitrogen-rich precursors.¹⁰

We have devised a method to attempt to quench shock-induced decomposition products on an ultrafast time scale in an effort to observe the intermediate species of a shock-induced decomposition. In these experiments, a shock wave compresses

Received: February 22, 2012

Revised: May 1, 2012

Published: May 3, 2012



the material of interest to a state of elevated temperature and pressure (~ 40 – 60 GPa), leading to decomposition of the constituent molecules. This chemistry is subsequently quenched after approximately several hundred picoseconds by a rarefaction or a release wave that relaxes the extreme pressures of shock compression to a density similar to ambient conditions. Ideally, the brevity of the shock compression allows enough time to begin the initial decomposition reactions and the early stages of carbon condensation, without allowing a full progression to the final decomposition products.

This article describes the shock-induced decomposition experiments of confined ultrafine TATB and the X-ray photoelectron spectroscopy (XPS) and the vibrational spectroscopy results obtained from recovered reaction products. For comparison, we have also prepared and characterized an amorphous carbon nitride material.

2. EXPERIMENTAL METHODS

2.1. Sample for Ultrafast Shock Compression. Ultrafine TATB powder was obtained from LLNL and used without any further processing. For the shock-induced decomposition experiments, post mortem analysis of the reaction products was the primary interest; thus, the TATB sample was confined in a diamond-anvil cell (DAC) to prevent loss of solid-phase reaction products from unrestricted material ablation. The DAC system modified for shock compression has been described previously.¹¹ In this experiment, one of the diamond anvils of a standard DAC was replaced with a sapphire anvil covered with a ~ 1 μm thick aluminum ablation layer, making an $\text{Al}_2\text{O}_3/\text{Al}/\text{TATB}/\text{diamond}$ sandwich. The TATB sample was compressed in the DAC without the use of a gasket to a minimal pressure, ~ 1 GPa, to produce a well-packed sample and to minimize voids. Uniaxial pressure of 207 MPa applied to ultrafine TATB powder reaches densities between 1.80 and 1.86 g/cm^3 , which is 93% to 95% of the theoretical maximum density (TMD).¹² With the application of ~ 1 GPa of uniaxial pressure, we would expect a density closer to the TMD. The sample thickness near the edge of the diamond culet was measured using interferometry to be between 2 and 3 μm thick.

2.2. Shock Generation. The ultrafast shock-compression apparatus, depicted in Figure 1, has been recently discussed in

detail.¹¹ The laser system is a chirped pulse amplified laser system comprised of a Mira oscillator, a Legend regenerative amplifier, and a custom, home-built stretcher and pulse shaper. The output pulse has a ~ 300 ps duration, a ~ 10 ps leading-edge rise time, a center wavelength of ~ 800 nm, and contains up to ~ 300 μJ of energy. As shown in Figure 1, the pump pulse, attenuated to ~ 100 μJ , was focused through the sapphire anvil to a spot size of ~ 20 μm (fwhm) on the aluminum layer. The absorbed pulse energy leads to plasma expansion of the aluminum layer, generating a shock wave that travels away from the plasma through the remaining intact aluminum and then into the TATB sample. Because the shock wave is generated by a laser pulse with a Gaussian intensity profile, the wave has a two-dimensional structure, characterized by a given peak stress and width. Previous studies of well-characterized ultrafast shock compression of similar aluminum films conducted with this apparatus suggest that the peak compressional stress within the aluminum films for the experimental parameters of the current study are between 40 and 60 GPa.¹³

The sample was confined within a modified DAC chamber and then subjected to shock compression. Because of the difference in size between the aluminum-coated sapphire culet, 400–500 μm , and the pump pulse fwhm, ~ 20 μm , the entire TATB sample was shock compressed with an array of spatially distinct compression events. The central points of individual shocks were spaced apart by 30 μm to prevent the overlap of compression events.

2.3. Thermal Pyrolysis. Thermal pyrolysis of TATB, employing a similar method to that of Pels et al., was used to produce a nitrogen-rich carbon material.¹⁴ Approximately 2 mg of ultrafine TATB powder was placed in a nonreactive platinum boat and heated to 400 $^\circ\text{C}$ under a dry N_2 atmosphere for 35 min. After which, the sample was left to cool without assistance. The resultant TATB char was black in color.

2.4. Raman Spectroscopy. Raman spectra were collected in a backscatter geometry using the 632.8 nm line from a helium–neon laser as the excitation source with a typical power of ~ 0.3 mW and focused to an ~ 20 μm full-width at half-maximum (fwhm) spot. The collected Raman scattered light was focused onto a 25 μm slit of an ISA SPEX HR-460 spectrograph, dispersed with a 300 groove/mm grating and finally detected with a $I\text{-N}_2$ cooled Roper Scientific CCD. An absolute wavelength calibration was obtained using the emission lines of Ne.

Spectra at various positions were collected for all samples to ensure spatial homogeneity. Additionally, several spectra were taken at the position, having various fluences, to test for laser-induced damage; none was observed. Both the preshock spectra of TATB and spectra of shock-induced decomposition products were gathered through the diamond side of the DAC with the sample under static compression. The Raman scattering from the diamond was suppressed with the aid of confocal spatial filtering.

2.5. $\mu\text{-FTIR}$ Spectroscopy. The FTIR spectra were collected with a Bruker Optics Vector-33 interferometer modified to provide spatial resolution on the order of tens of micrometers. InSb and HgCdTe detectors provide sensitivities across the vibrational regions of interest. Each spectrum was a coaverage of 100 scans with a 2 cm^{-1} resolution. Powder samples were placed on to a NaCl window substrate.

2.6. X-ray Photoelectron Spectroscopy. X-ray photoelectron spectroscopy (XPS) was performed on a PHI Quantum 2000 system using a focused monochromatic Al

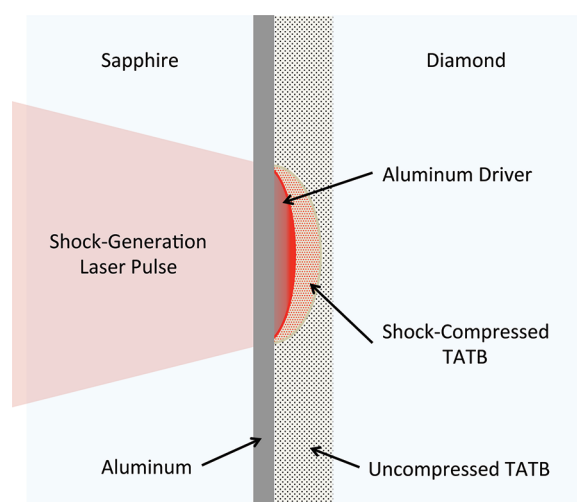


Figure 1. Cartoon depicting shock-induced chemistry within the TATB sample. This figure is not to scale. Approximately 500 shots were conducted to produce enough recovered material for analysis.

K α X-ray (1486.7 eV) source for excitation and a spherical section analyzer. The instrument has a 16-element multi-channel detection system. A 100 μm diameter X-ray beam was used for analysis. The X-ray beam is incident normal to the sample and the X-ray detector is at 45° away from the normal. The pass energy was 23.5 eV giving an energy resolution of 0.5 eV that, when combined with the 0.85 eV fwhm Al K α line width, gives a resolvable XPS peak width of 1.3 eV fwhm. Deconvolution of nonresolved peaks was accomplished using Multipak 9.2 (PHI) curve fitting routines with a Shirley background. The collected data were referenced to an energy scale with binding energies for Cu 2p $_{3/2}$ at 932.72 ± 0.05 eV and Au 4f $_{7/2}$ at 84.01 ± 0.05 eV. Samples were placed on indium foil and the In 3d $_{5/2}$ peak of In $_2$ O $_3$ at 444.7 eV served as a charge reference for each sample.¹⁵ The use of charge compensation beams to reduced sample charging was not required for either the pyrolyzed TATB or the shocked TATB samples.

3. RESULTS

3.1. Vibrational Spectroscopy. **3.1.1. TATB.** The infrared and Raman spectra of the ultrafine TATB under static compression, shown in Figures 2 and 3, are similar to that

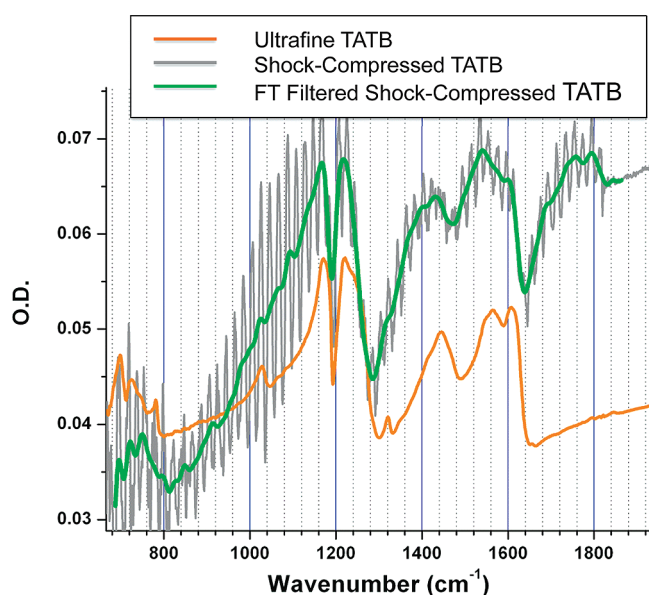


Figure 2. Comparison of infrared spectra of ultrafine TATB (orange) and raw shock-compressed TATB (black). The raw spectrum of the shock-compressed TATB contains etaloning, which has been Fourier filtered for clarity (green). The intensity scale of the ultrafine TATB spectrum was adjusted to facilitate comparison between shock-compressed TATB.

observed in other works.^{16–18} The vibrational modes of TATB at room temperature and ambient pressure are best displayed by the high-resolution spectra of McGrane et al.¹⁷ Our Raman spectra are broadened primarily by the low resolving power of the 300 groove/mm grating used here to obtain the full Stokes region between 200 and 3600 wavenumbers in a single spectrum. The vibrational features here are additionally broadened by the application of nonhydrostatic pressure.¹⁹ We are not attempting to provide any new insight to the fundamental spectrum of TATB and only show it as a comparison for the reacted TATB samples.

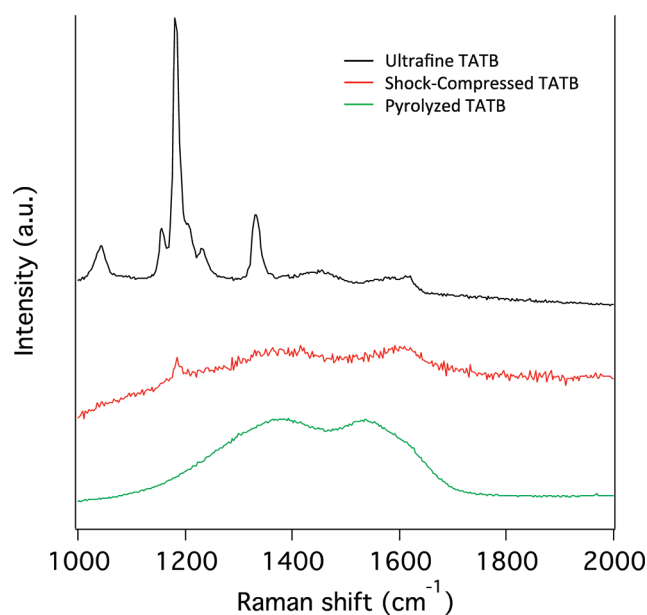


Figure 3. Raman spectra of ultrafine TATB (top), shock-compressed TATB (middle), and pyrolyzed TATB (bottom). The data have been corrected for acquisition duration and are offset for clarity.

3.1.2. Pyrolyzed TATB. Neither the Raman spectrum, Figure 3, nor the FTIR spectrum, Figure 4, of the thermally pyrolyzed

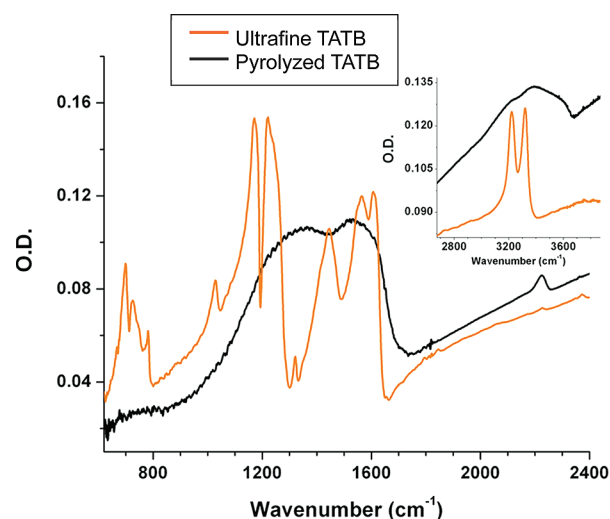


Figure 4. Comparison of infrared spectra for ultrafine TATB (orange) and pyrolyzed TATB (black) samples. The ultrafine TATB spectrum is the same as that of Figure 2. The insert shows the C–H stretching region.

TATB sample share any spectral similarities with that of TATB. Instead, both exhibit two broad features in the 1300–1600 cm^{-1} spectral region, both have fwhms between 200 to 300 cm^{-1} . These peaks are consistent with the well-known vibrational features, the *D* peak and the *G* peak, observed in both carbon and carbon nitride materials.^{20–22} Both features are attributed to the vibrations of sp^2 structures; the *D* peak, ~ 1360 cm^{-1} , is ascribed to a bending motion, while the *G* peak at ~ 1560 cm^{-1} is assumed to arise from motion dominated by stretching.

The *D* and *G* bands have slightly different shapes and peak positions in the infrared and Raman spectra. The infrared

absorption and Raman scattering processes are fundamentally different and probe similar functional groups with differing sensitivity. Furthermore, the excitation wavelength of the Raman probe is known to affect both the positions (relative cm^{-1}) and intensities of these bands for these materials.²²

3.1.3. Shock-Compressed TATB. Shown in Figure 3, small amounts of unreacted TATB were observable in the Raman spectra, depending on the sample area probed. Shown here is a spectrum with a contribution from TATB with the shock-induced decomposition products representative of the material. On the basis of the absolute strength of the TATB peaks and the relative acquisition times, we estimate that only a few percent of the surface molecules remained unchanged.

Two broad features similar to that of the *D* and *G* bands are observed but with very weak intensities compared to the pyrolyzed TATB. As discussed previously, the *D* and *G* peaks are characteristic of sp^2 structures, suggesting that the decomposition product contains sp^3 structures. There is a *T* peak at $\sim 1000\text{ cm}^{-1}$ that is attributed within the literature to an sp^3 carbon structure; however, this Raman feature is only observed with a UV excitation source.²²

While decomposition products dominate the Raman spectrum, the FTIR spectrum (Figure 2) retains a strong resemblance to the unreacted TATB. The apparent difference in the absolute absorbance between the two samples is likely an artifact of probing such small sample volumes. The appearance of new absorptions between 1300 and 1400 cm^{-1} , near 1550 cm^{-1} , and between 1700 and 1800 cm^{-1} and changes in the background shape indicate that some of the material underwent structural changes. Significant etalonning exists in this FTIR spectrum and was subsequently Fourier filtered out. Both spectra are shown. It should be noted that observed loss at 1320 cm^{-1} is real and not a result of the filtering process; this was tested by acquiring additional spectra.

3.2. XPS. To obtain any changes in both the relative atomic concentrations and the local bonding structures of that resulted from the various treatments of TATB, each sample was further analyzed by XPS. The results are discussed below.

3.2.1. TATB. Figure 5A shows the C 1s region of a partially resolved feature comprising two distinct species fit with binding energies of 285.1 and 286.4 eV was observed. Bonding to more electronegative atoms tends to shift the carbon binding energy to higher binding energies; thus, the 286.4 eV species is attributed to the C- NO_2 carbon, and the 285.1 eV species is then the C- NH_2 carbon. To our knowledge, this is the first time that these two carbons have been partially resolved. Previous work measured an unresolvable single feature with a reported fwhm of 3.55 eV .²³

The N 1s region, Figure 6A, of the TATB sample displays three features with binding energies of 398.3 , 404.0 , and 407.0 eV . These peaks are similar to those reported previously.²³ The 398.3 eV species is the $-\text{NH}_2$ nitrogen, the 404.0 eV peak is the main peak from the $-\text{NO}_2$ nitrogen, and the 407.0 eV peak is a satellite peak. The oxygen from the $-\text{NO}_2$ groups also results in the only features in the O 1s region as shown in Figure 7A. The main O 1s feature occurs at a binding energy of 531.1 eV and is accompanied by a satellite at 535.14 eV .

The binding energies for TATB reported in this study are $\sim 0.6\text{ eV}$ lower than those published by Sharma et al.²³ The seeming discrepancy can be ascribed to the charge correction method employed in each experiment. Sharma et al., while not stated explicitly, appears to have shifted the broad carbon feature to a binding energy of 285.0 eV . We have instead

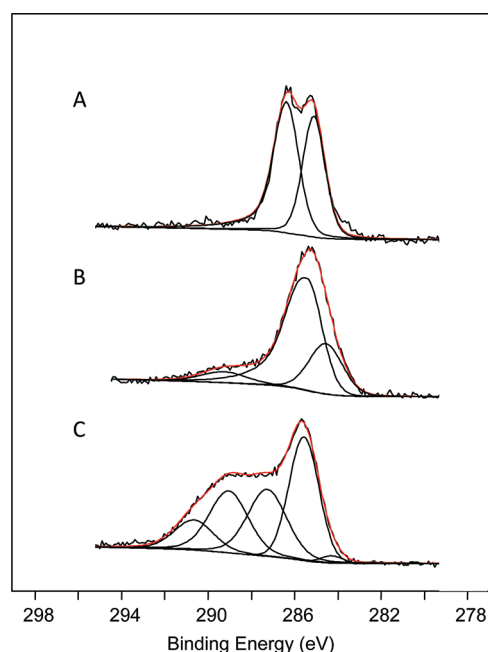


Figure 5. C 1s transitions for (A) ultrafine TATB, (B) pyrolyzed TATB, and (C) shock-compressed TATB. The ordinate axis is of arbitrary intensity, and the individual spectra are offset for clarity.

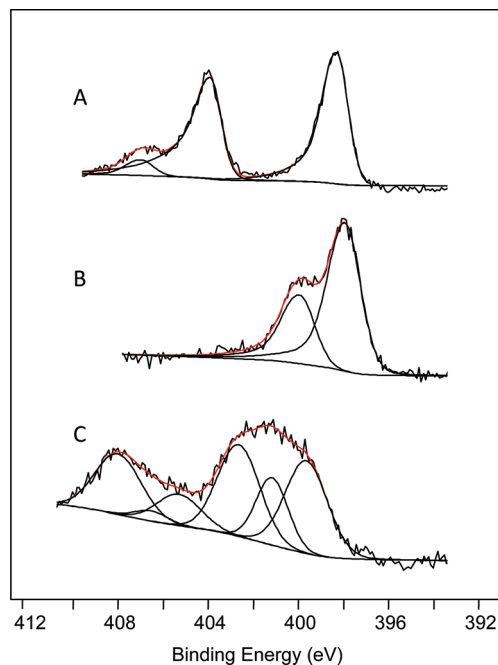


Figure 6. N 1s transitions for (A) ultrafine TATB, (B) pyrolyzed TATB, and (C) shock-compressed TATB. The ordinate axis is of arbitrary intensity, and the individual spectra are offset for clarity.

corrected the binding energy by shifting the In $3d_{5/2}$ of In_2O_3 , using a reference that is independent of the carbon in the TATB sample.

3.2.2. Pyrolyzed TATB. Quantitative analysis for the pyrolyzed TATB indicates that relative atomic composition is 66.9% carbon, 31.1% nitrogen, and 2.0% oxygen. The pyrolysis product is primarily carbon and nitrogen confirming the synthesis of a carbon nitride material. It is possible that oxygen presence is from atmospheric contamination during the transfer

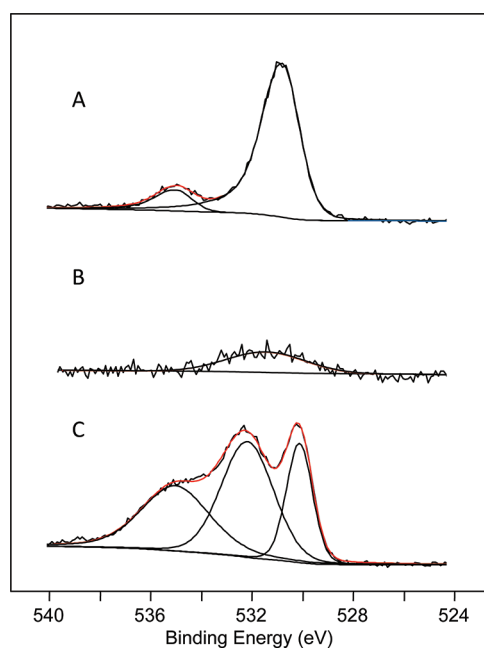


Figure 7. O 1s transitions for (A) ultrafine TATB, (B) pyrolyzed TATB, and (C) shock-compressed TATB. The ordinate axis is of arbitrary intensity and the individual spectra are offset for clarity.

process. Table 1 contains relative atomic concentrations for all samples.

Table 1. Relative Atomic Concentrations

	relative atomic concentrations (percent loss ^a)		
	carbon	nitrogen	oxygen
TATB ^b	0.33	0.33	0.33
pyrolyzed TATB	0.67	0.31 (54%)	0.02 (97%)
shocked TATB ^c	0.52	0.13 (75%)	0.35 (33%)

^aPercent loss is calculated with respect to the remaining carbon content. ^bNominal atomic concentrations for TATB. ^cRecalculated without In₂O₃ contributions in O 1s.

The main feature in the C 1s region, Figure 5B, for the pyrolyzed TATB sample is a broad, unresolved peak fit to three species, each having a fwhm of ~ 2.2 eV. These widths are larger than the spectrometer resolution of 1.3 eV and are likely the result of a manifold of species, characteristic of an amorphous

material. For simplicity, we have consciously chosen not to over fit the data and present only fits that are robust. The three components of the C 1s region have binding energies of 284.4, 285.4, and 289.4 eV and relative areas of 0.25, 0.67, and 0.08, respectively.

The N 1s binding region, Figure 6B, contains an asymmetric feature that can be fit to two nitrogen species with binding energies of 398.1 and 400.1 eV and with relative integrated intensities of 0.68 and 0.32. The absolute signal from the O 1s region, Figure 7B, is relatively low compared to the other regions. Correspondingly, the signal-to-noise is considerably worse; however, there is an observable broad peak centered about 531.8 eV with a ~ 3.7 eV fwhm. Such a large peak width suggests that this feature is two peaks.

3.2.3. Shock-Compressed TATB. Quantitative analysis from the survey spectrum for the shock compressed TATB sample shows that relative atomic composition is 46.7% carbon, 12.2% nitrogen, and 41.1% oxygen. Approximately 75% of the original nitrogen atoms were liberated as gas-phase products as a result of the compression event. The relative oxygen concentration is elevated from contributions from In₂O₃; 23.3% of the oxygen is from In₂O₃.

The features for both the C 1s and the N 1s regions for the shock-compressed TATB sample are quite rich with respect to both the ultrafine TATB and the pyrolyzed TATB. The pyrolyzed and shock-compressed TATB samples are similar in that the individual components used to fit unresolved features tend to have fwhms in excess of the instrument resolution; again, this can be attributed to an existence of a manifold of species from an amorphous material. As a fitting guide, the fwhm of each component was kept below ~ 2.2 eV, which resulted in reasonable fits.

The C 1s spectral region, Figure 5C, was fit to five separate species with binding energies of 284.1, 285.4, 287.2, 289.0, and 290.7 eV with relative respective contributions of 0.02, 0.34, 0.27, 0.25, and 0.12. The N 1s region, Figure 6C, was fit to a total of six components at 399.7, 401.3, 402.7, 405.4, 406.6, and 408.1 eV with relative integrated intensities of 0.27, 0.15, 0.27, 0.09, 0.02, and 0.19, respectively. The O 1s region, Figure 7C, was fit with three subpeaks with binding energies of 530.1, 532.2, and 535.0 eV and relative integrated intensities of 23.3%, 44.0%, and 32.7%, respectively.

Table 2. XPS Peak Positions and Assignments

	orbital	peak position (eV)	comment		orbital	peak position (eV)	comment
TATB	C(1s)	285.1	C-NH ₂	shocked TATB	C(1s)	284.1	sp ² C-C
	C(1s)	286.4	C-NO ₂		C(1s)	285.4	sp ³ C-C
	N(1s)	398.3	-NH ₂		C(1s)	287.2	C-N
	N(1s)	404.0	-NO ₂		C(1s)	289.0	R-COOH
	N(1s)	407.0	satellite		C(1s)	290.7	R-OCOO-R
	O(1s)	531.1	-NO ₂		N(1s)	399.7	R-N=O, R-NH ₂ , C-N
	O(1s)	535.14	satellite		N(1s)	401.3	R-N=O
	C(1s)	284.4	sp ² C-C		N(1s)	402.7	R-N=O
pyrolyzed TATB	C(1s)	285.4	sp ² C-N		N(1s)	405.4	R-NO ₂
	C(1s)	289.4	R-COOH		N(1s)	406.6	R-NO ₂
	N(1s)	398.1	R-NH ₂		N(1s)	408.1	R-O-NO ₂
	N(1s)	400.1	N-5 C-N		O(1s)	532.2	R-N=O, R-COOH
	O(1s)	531.8	R-COOH, In ₂ O ₃		O(1s)	535.0	H ₂ O

4. DISCUSSION

The possibility that carbon nitrides would be recovered from the quenched ultrafast shock-induced decomposition lead us to synthesize a carbon nitride material to use as a reference, and accordingly, the pyrolyzed TATB will be quickly discussed, followed by a more in-depth discussion of the shock-compressed TATB.

4.1. Pyrolyzed TATB. The XPS results indicate that the pyrolyzed sample is indeed dominated by carbon and nitrogen. The Raman spectrum also suggests that the material is dominated by sp^2 structures, opposed to an sp^3 -dominated carbon nitride. In fact, the 900–1800 cm^{-1} region of the FTIR spectrum of the pyrolyzed TATB sample strongly resembles the a-CN films sputter deposited at elevated substrate temperatures and 150 W of RF power.²⁴ While, the 500–3500 cm^{-1} region of the Raman spectrum is quite similar to that of the amorphous carbon nitrides deposited with 50 W of RF power and an elevated substrate temperature.

Guided by the Raman spectroscopy, both chemical species observed in the C 1s and N 1s regions can now be assigned. The 284.5 eV component in the carbon spectrum is a graphite-like carbon, i.e., an sp^2 carbon species bound only to other carbons. Graphite has a binding energy reported between 284.4 and 284.6 eV, while sp^3 -hybridized carbon materials have binding energies ~ 0.9 eV higher.^{25–27} Given the amount of nitrogen present in this material, the 285.4 eV C 1s subpeak must be an sp^2 carbon bound to nitrogen and not an sp^3 species.²⁸ The broad 289.4 eV subpeak contains the carboxylic-acid carbon, observed in the Raman spectrum, along with contribution from a manifold of π -type shakeup satellites.²⁹ Table 2 summarizes the binding energies and assignments for all samples.

The XPS N 1s region exhibits two species of which, directed by the Raman spectrum, one of them must be related to an NH_2 functional groups. The 398.1 eV component would then correspond to a NH_2 group, based on an electronegativity argument. This binding energy is quite similar for the NH_2 group in TATB. The other nitrogen species with a binding energy of 400.1 eV has been fully incorporated into the carbon network. The designations for these types of nitrogen are N-5, N-6, or N-Q, where an N-5 or N-6 nitrogen occupies an edge site of an sp^2 carbon sheet as a heteroatom within a 5- or 6-membered ring, respectively, and an N-Q nitrogen populates an interior site of the carbon sheet with three carbon–nitrogen bonds.¹⁴ Following the assignments of Pels et al., the 400.1 eV species of the pyrolyzed TATB is likely an N-5 nitrogen flavor. For a direct comparison, the binding energies of Pels et al. were shifted such that the sp^2 C 1s peak corresponds to graphite (284.4 eV) and not the reported 285.0 eV.

4.2. Shocked TATB. The changes evidenced in the XPS and vibrational spectra of the decomposition products provide verification that a substantial amount of shock-related chemistry occurred. This is quite different than previous shock-induced chemistry studies of TATB conducted at much lower shock stresses, where less dramatic changes in the XPS spectra were observed.^{30,31}

The carbon species with binding energies of 284.1 and 285.5 eV can be rationalized as sp^2 and sp^3 amorphous carbon.²⁷ Amorphous sp^3 carbon would not display strong D or G bands in a Raman spectrum,²² explaining the order-of-magnitude intensity difference in that spectral region between the pyrolyzed TATB and shock-compressed TATB. A disordered sp^3 structure, such as an ion-etched diamond surface also has a

reported C 1s binding energy of 285.4 eV,²⁵ similar to that observed in this work. An amorphous carbon material would not have a sharp Raman feature characteristic of an ordered diamond structure. The binding energy for the sp^2 -hybridized carbon is ~ 0.3 eV lower than expected.^{25,32} We attribute this discrepancy to fitting uncertainty of such a minor species.

The 287.2 eV component agrees well to carbon species bound to a nitrogen atom.²⁶ The binding energy of the two carbon atoms directly bonded to the nitrogen atoms in furoxan molecules have binding energies of ~ 287 eV, this is inferred from the XPS spectra of Kim et al. before and after the electron-beam-mediated removal of the furoxan moiety.³³ The integrated intensity for this carbon peak corresponds to $\sim 12.5\%$ of the total number of surface atoms, which is quite similar to the $\sim 12.2\%$ of surface atoms that correspond to nitrogen atoms. Oxidized carbons in the form of carboxylic acids of organic carbonate species are reasonable assignments for the C 1s binding energies of 289.0 and 290.8 eV.²⁶

The N 1s binding region is congested with numerous overlapping components, which hinders our ability to make more definitive assignments. This problem is compounded by the near-featureless Raman spectrum for this sample. These peaks are consistent with various organic forms of oxidized nitrogen. Nitroso molecules have N 1s binding energies that span from 399.7 to 403.8 eV.³⁴ Nitroxooxy, nitro and nitrate molecules extend this range up to 408.1 eV.^{26,35} Furoxans and furazans are thought to be molecular intermediates of shock-induced decomposition events.³¹ The binding energy for furazan-specific nitrogen varies between 399.6 and 401.5 eV, and for the furoxan-specific nitrogen, it ranges from 403.8 to 404.5 eV, depending on the larger structure of the material.^{31,33}

Our discussion of nitrogen species directly bonded to oxygen atoms does not preclude the presence of other organic functionalities. There are a variety of different amides and amines that would also be consistent with lower binding-energy species.²⁶ Additionally, the 399.7 eV component is similar to that observed for low nitrogen-content carbon nitrides. For simplicity, we have tried to guide our assignments with previous thermal decomposition experiments, which indicate that most of the decomposition products are oxidized.³⁶ The major product Land et al. observed in their thermal decomposition studies was NO. A nitroso functional group would be a reasonable precursor structure to facilitate NO loss. Furthermore, the infrared absorption spectrum displays absorption loss near 1320 cm^{-1} and an increase around 1550 cm^{-1} that supports the conversion of nitro groups into nitroso groups.³⁷

The O 1s region is consistent with the presence of the discussed oxidized carbon and nitrogen forms. The oxygen binding energies for the nitroso molecules are between 531.7 and 534.1 eV in good agreement with our data.³⁴ The 532.2 eV peak is broad and likely not a single species but a manifold of related species. Moreover, the oxygen atoms from the carboxylic acid and carbonate functional groups fall into a similar ~ 532 and ~ 534 eV region. The 530.1 eV oxygen feature is from the In_2O_3 foil. The third general feature with a binding energy of 535.0 eV is water with various degrees of hydrogen bonding.³⁸ We have no absolute answer about whether or not this water is a decomposition product or an atmospheric contaminant, but we do note that the shock-compressed TATB contains significantly more water than other samples that were stored under similar conditions.

4.3. Origin of Decomposition Products. Haskins et al. have proposed an extended phenomenological model of shock-

induced ignition and reaction growth of energetic materials, which is capable of reproducing the behavior of both homogeneous and heterogeneous materials for impact events on nanosecond and microsecond time scales.³⁹ The characteristic time to achieve detonation is separated into two separate contributions; ignition, which describes the time delay while the initial shock-induced chemistry occurs, modeled using single step Arrhenius kinetics; and the growth time, which designates the time required to generate a self-sustaining exothermic reaction that results in a detonation event. The growth period before the onset of detonation would be ~ 5 ns for the shock compression stress obtained in the current experiments, a duration $17\times$ longer than the actual shock compression. However, the ignition time scale is calculated to be either on the order of 1 or 10 ps, depending on the exact applied shock stress applied in the current work. This calculation relies on an extrapolation of the initiation model by several orders of magnitude in time (nanoseconds to picoseconds) past the supporting data. An ignition time of tens of picoseconds is close to the physically realistic limit for a thermally driven reaction that follows Arrhenius kinetics. The ignition time scale is well matched to the shock duration of these ultrafast shock-quenched experiments.

The shock strength or the applied compression stress of these experiments is well above the Chapman–Jouguet pressure, ~ 29 GPa, for steady-state detonation of TATB.⁴⁰ However, since we are concerned with shock-induced ignition, a more appropriate comparison is to the von Neumann spike pressure, which is the actual pressure of the leading edge of the detonation wave; these are the conditions that initiate shock-induced chemistry during detonation. For TATB, the pressure for the von Neumann spike is ~ 34 GPa,⁴¹ still significantly lower than the experimental conditions of this work. Accordingly, the shock-induced decomposition products observed here should be viewed as ignition-like decomposition products of a significantly overdriven wave.

Even though the stress of shock compression is quenched on an ultrafast time scale, the nonadiabatic nature of shock compression leads to nonreversible energy deposition, leading to an elevated temperature. Furthermore, the aluminum ablation layer, after absorbing laser energy, would also exhibit an elevated temperature. Pending the relief of this extra thermal energy by heat transport on the microsecond time scale, this elevated temperature will persist and may lead to further thermal decomposition of unreacted TATB. This sustained temperature may result in the observation of products from two distinct conditions: an elevated pressure and temperature condition during shock compression or an elevated temperature after the rarefaction wave arrival.

There is experimental evidence that provides credibility that the observed decomposition is actual shock-induced chemistry. The infrared spectra of the TATB before and after shock compression are remarkably similar above 1000 cm^{-1} and implies that the bulk of the shock compressed material is primarily unreacted. The Raman spectra of TATB before and after shock compression are, however, considerably different. These Raman spectra were collected from the diamond side of the DAC, the side opposite that of the shock generation side. This indicates that the chemistry occurred preferentially at the TATB/diamond interface where the shock wave was partially reflected as a consequence of the interfacial shock impedance mismatch. Figure 8 presents the pertinent Hugoniot data and the impedance matching for this system.^{42,43} This reflected

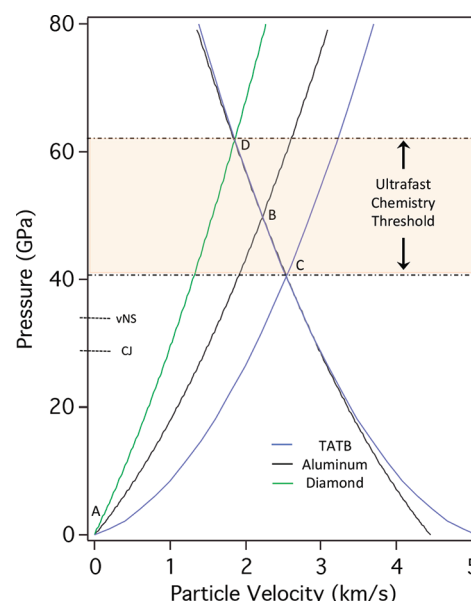


Figure 8. Description of impedance matching and the evolution of the shock compression of this system. The Hugoniot data was obtained from refs 39 and 40. A laser-generated shock takes the aluminum from point A to a shock pressure of ~ 50 GPa at point B along a straight Raleigh line. Because of an impedance mismatch of the Al and TATB, the shock transmitted into the TATB is ~ 40 GPa, and the aluminum compression is relieved along the aluminum isentrope from point B to point C, as a relaxation wave is launched backward into the aluminum material. As the shock wave propagates through the TATB material, a ~ 40 GPa stress is maintained. Once the wave reaches the TATB/diamond interface, the impedance mismatch causes the shock to partially reflect back into the TATB, pushing the TATB state along a Raleigh line from point C to point D. A portion of the TATB remains at ~ 60 GPa for ~ 150 ps until the pressure is relieved back to ~ 0 GPa by a rarefaction wave. Shock-induced chemistry was observed to occur between peak pressures of ~ 40 – 60 GPa on an ultrafast time scale. Also shown are the Chapman–Jouguet (CJ) and von Neumann spike (vNS) pressures for comparison.

wave would raise the peak pressure from ~ 40 GPa to ~ 60 GPa for ~ 150 ps until the arrival of the rarefaction wave relaxed the pressure. These pressures may bound either the endothermic steps or the ignition threshold for ultrafast shock-induced decomposition for TATB.

The solid carbon observed in the shock compressed TATB is highly likely a shock-compression product. The weak D and G Raman peaks along with a carbon species with a binding energy of 285.4 eV , suggests that the solid carbon product is primarily both sp^3 and amorphous in nature. There is no precedent for the formation of sp^3 carbon from either deflagration or pyrolysis of an organic precursor at static pressures of ~ 1 GPa. Diamond is the thermodynamically favored state of carbon under the ~ 60 GPa peak shock pressure of this study,⁴⁴ and detonation-based nanodiamond synthesis is an established process.⁴⁵ Interestingly, we do not observe the $\sim 1326\text{ cm}^{-1}$ Raman signature for nanodiamonds,⁴⁶ suggesting that either the formation of well-ordered sp^3 structures occurs on time scales greater than ~ 150 ps or that nanodiamonds do not form under these shock conditions.⁴⁷

The remaining TATB decomposition products likely originate from regions periphery to the peak compressional stress. The XPS X-ray source has a diameter of $100\text{ }\mu\text{m}$ and probed a sample area containing several shock events.

Furthermore, the shock pressure decays radially away from the peak stress and not all TATB molecules received the same absolute compression. It is quite possible that this material has experienced a relatively mild compression event and is in the early stages of decomposition. A realistic shock stress for a TATB molecule located a radial distance of $\sim 15\ \mu\text{m}$ from the peak stress predicts an ignition time of $\sim 50\ \text{ps}$, based on the model of Haskins et al.^{11,39} The alternative is that these decomposition products have primarily undergone thermal decomposition after the arrival of the rarefaction wave or a combination of both. However, if this was the case and a majority of the decomposition occurred after the rarefaction wave, then one should expect to have observed significant decomposition of the entire TATB sample, not just the TATB nearest the diamond interface.

4.4. Comparison to Molecular Dynamics Simulations.

Regardless of the whether these molecules decomposed under shock compression, the nitrogen-containing products observed are consistent with the loss of water. A majority of the nitrogen atoms exist in an oxidized form similar to either nitroso-related molecules or, possibly, the previously proposed furoxan and furazan molecules.^{36,31} Additionally, a significant amount of water was observed in the XPS data, which is similar to the simulations that predict an abrupt loss of water within $\sim 20\ \text{ps}$.⁷

It is possible that carbon nitride materials are present in the shock-compressed TATB. A fraction of the nitrogen atoms have a binding energy (399.7 eV) that is consistent with previous carbon nitride studies.³² At this point, the existence of carbon nitrides as a product species cannot be either confirmed or ruled out. We can say with confidence that $\sim 75\%$ of the remaining nitrogen species have binding energies inconsistent with previous amorphous carbon nitride studies. Additionally, the nitrogen-rich heterocyclic rings depicted in Manaa et al. are dominated by sp^2 -hybridized structures suggesting that the nitrogen would be similar to N-5, N-6, or N-Q type; however, none of the nitrogen atom binding energies match well to these nitrogen types.¹⁴

One important difference between the simulations and the experiment is the influence of temperature on the reactions. While the shock-induced temperature increase in the experiment is not measured directly, we expect a temperature increase that is consistent with the shock-compression process. Accordingly, for similar particle velocities and material densities, the simulations and experiment would be expected to reach similar temperatures. While the experimental density was not measured, it is reasonable to assume that the densities are similar to within a few percent. The bulk of the shock-compressed TATB appears to be primarily unreacted despite these high temperatures, suggesting that, on these time scales, temperature alone does not induce thermal decomposition of TATB. However, it is quite possible that the shock-induced decomposition continues at the elevated temperatures after the shock pressure is relieved for those molecules at the diamond interface. If this is the case, the recovered shock-induced decomposition products in the current experiments are related to, but not directly comparable to, the products observed in the simulations.

Both this work and the simulations of Manaa et al. are overdriven with pressures roughly twice the detonation pressures for TATB. Even if a definitive observation of either carbon nitrides or the nitro-rich heterocycles were to occur, whether or not this process is of consequence for an actual detonation process is not straightforward. Future work might

include trying to observe the nitrogen content in recovered detonation products of pure TATB quenched by a pressurized inert atmosphere.

5. CONCLUSIONS

We believe that we have observed shock-induced decomposition intermediates of TATB that have been quenched. These decomposition intermediates include amorphous carbon with a primarily sp^3 -dominated structure along with other oxidized carbon and nitrogen species. Shock compression of TATB at the diamond interface resulted in a loss of $\sim 35\%$ and $\sim 75\%$ of the oxygen and nitrogen atoms to gas-phase products, respectively. The majority of the remaining nitrogen appears to be oxidized as nitroso, nitro, and nitrate species, while the oxygen arises from water, carboxylic acid groups, carbonates, and the previously mentioned nitrogen oxides. To our knowledge, this is the first time that nitroso-based molecules have been associated with shock-induced decomposition for TATB.

Our experimental results neither confirm nor disprove the predictions that nitrogen-rich heterocyclic rings impede the energy release during the detonation of TATB. The shock-compressed TATB and the pyrolyzed TATB are quite different in both their vibrational spectra and the atomic binding energies, suggesting that amorphous carbon nitride was not a major component of the shock-induced reactions. We did, however, observe chemistry that occurred preferential at the TATB/diamond interface where a reflected shock wave would further increase the shock pressure temporarily. This was interpreted as an indirect measurement of the required pressure that leads to the early stages of ignition on the ultrafast time scale; the threshold for reaction on the time scale of this experiment corresponds to peak pressures greater than ~ 40 and less than $\sim 60\ \text{GPa}$.

AUTHOR INFORMATION

Corresponding Author

*E-mail: carter64@llnl.gov.

Notes

The authors declare no competing financial interest.

ACKNOWLEDGMENTS

We acknowledge Dr. Sorin Bastea and Dr. Craig Tarver for helpful discussions and guidance. This research was supported by the DOE Champaign_II and Joint DoD/DOE Munition Technology Programs and performed under the auspices of the U.S. Department of Energy by Lawrence Livermore National Laboratory under contract DE-AC52-07NA27344.

REFERENCES

- (1) Mader, C. L. *Numerical Modeling of Detonation*; University of California: Berkeley, CA, 1979.
- (2) Ree, F.; Viecelli, J.; van Thiel, M. Influence of fluorine chemistry on supercritical fluid-fluid phase separations. *J. Mol. Liq.* **2000**, *85* (1–2), 229–236.
- (3) Shaw, M.; Johnson, J. Carbon clustering in detonations. *J. Appl. Phys.* **1987**, *62* (5), 2080–2085.
- (4) Nomura, Y.; Kawamura, K. Soot derived from the detonation of a trinitrotoluene charge. *Carbon* **1984**, *22* (2), 189–191.
- (5) Greiner, N.; Phillips, D.; Johnson, J.; Volk, F. Diamonds in detonation soot. *Nature* **1988**, *333* (6172), 440–442.
- (6) Sorin, B. Private communication, December 16th, 2011.

- (7) Manaa, M.; Reed, E.; Fried, L.; Goldman, N. Nitrogen-rich heterocycles as reactivity retardants in shocked insensitive explosives. *J. Am. Chem. Soc.* **2009**, *131* (15), 5483–5487.
- (8) Odintsov, V.; Pepekin, V. Estimation of thermodynamic stability conditions and perspectives for synthesis of covalent carbon nitride. *Propellants, Explos., Pyrotech.* **1997**, *22* (1), 34–37.
- (9) Liu, A.; Cohen, M. Structural-properties and electronic-structure of low-compressibility materials: beta-Si₃N₄ and hypothetical beta-C₃N₄. *Phys. Rev. B* **1990**, *41* (15), 10727–10734.
- (10) Liu, J.; Sekine, T.; Kobayashi, T. A new carbon nitride synthesized by shock compression of organic precursors. *Solid State Commun.* **2006**, *137* (1–2), 21–25.
- (11) Armstrong, M.; Crowhurst, J.; Bastea, S.; Zaug, J. Ultrafast observation of shocked states in a precompressed material. *J. Appl. Phys.* **2010**, *108*, 2.
- (12) Gagliardi, F. J. Private communication, April 26th, 2012.
- (13) Crowhurst, J.; Armstrong, M.; Knight, K.; Zaug, J.; Behymer, E. Invariance of the dissipative action at ultrahigh strain rates above the strong shock threshold. *Phys. Rev. Lett.* **2011**, *107* (14), 144302.
- (14) Pels, J.; Kapteijn, F.; Moulijn, J.; Zhu, Q.; Thomas, K. Evolution of nitrogen functionalities in carbonaceous materials during pyrolysis. *Carbon* **1995**, *33* (11), 1641–1653.
- (15) Acacia, N.; Barreca, F.; Barletta, E.; Spadaro, D.; Curro, G.; Neri, F. Laser ablation synthesis of indium oxide nanoparticles in water. *Appl. Surf. Sci.* **2010**, *256* (22), 6918–6922.
- (16) Deopura, B.; Gupta, V. Vibration spectra of 1,3,5-triamino-2,4,6-trinitrobenzene. *J. Chem. Phys.* **1971**, *54* (9), 4013.
- (17) McGrane, S.; Shreve, A. Temperature-dependent Raman spectra of triaminotrinitrobenzene: Anharmonic mode couplings in an energetic material. *J. Chem. Phys.* **2003**, *119* (12), 5834–5841.
- (18) McGrane, S.; Barber, J.; Quenneville, J. Anharmonic vibrational properties of explosives from temperature-dependent Raman. *J. Phys. Chem. A* **2005**, *109* (44), 9919–9927.
- (19) Piermari, G. J.; Block, S.; Barnett, J. D. Hydrostatic limits in liquids and solids to 100 kbar. *J. Appl. Phys.* **1973**, *44* (12), 5377–5382.
- (20) Kleinsorge, B.; Ferrari, A.; Robertson, J.; Milne, W.; Waidmann, S.; Hearne, S. Bonding regimes of nitrogen in amorphous carbon. *Diamond Relat. Mater.* **2000**, *9* (3–6), 643–648.
- (21) Rodil, S.; Ferrari, A.; Robertson, J.; Milne, W. Raman and infrared modes of hydrogenated amorphous carbon nitride. *J. Appl. Phys.* **2001**, *89* (10), 5425–5430.
- (22) Ferrari, A.; Rodil, S.; Robertson, J. Interpretation of infrared and Raman spectra of amorphous carbon nitrides. *Phys. Rev. B* **2003**, *67* (15), 155306.
- (23) Sharma, J.; Garrett, W.; Owens, F.; Vogel, V. X-ray photoelectron study of electronic-structure and ultraviolet and isothermal decomposition of 1,3,5-triamino-2,4,6-trinitrobenzene. *J. Phys. Chem.* **1982**, *86* (9), 1657–1661.
- (24) Therasse, M.; Benlahsen, M. Effects of deposition temperature on the structure of amorphous carbon nitride films. *Solid State Commun.* **2004**, *129* (2), 139–142.
- (25) Lascovich, J.; Giorgi, R.; Scaglione, S. Evaluation of the sp²/sp³ ratio in amorphous-carbon structure by XPS and XAES. *Appl. Surf. Sci.* **1991**, *47* (1), 17–21.
- (26) Moulder, J. F.; Stickle, W. F.; Sobol, P. E.; Bombon, K. D. *Handbook of X-ray Photoelectron Spectroscopy*; Perkin-Elmer Corp.: Eden Prairie, MN, 1992.
- (27) Haerle, R.; Riedo, E.; Pasquarello, A.; Baldereschi, A. sp(2)/sp(3) hybridization ratio in amorphous carbon from C 1s core-level shifts: X-ray photoelectron spectroscopy and first-principles calculation. *Phys. Rev. B* **2002**, *65* (4), 045101.
- (28) Kessel, R.; Schultze, J. Surface analytical and photoelectrochemical investigations of conduction polymers. *Surf. Interface Anal.* **1990**, *16* (1–12), 401–406.
- (29) Leiro, J.; Heinonen, M.; Laiho, T.; Batirev, I. Core-level XPS spectra of fullerene, highly oriented pyrolytic graphite, and glassy carbon. *J. Electron Spectrosc. Relat. Phenom.* **2003**, *128* (2–3), 205–213.
- (30) Sharma, J.; Owens, F. XPS study of UV and shock decomposed triamino-trinitrobenzene. *Chem. Phys. Lett.* **1979**, *61* (2), 280–282.
- (31) Sharma, J.; Forbes, J.; Coffey, C.; Liddiard, T. The physical and chemical nature of sensitization centers left from hot-spots caused in triaminotrinitrobenzene by shock or impact. *J. Phys. Chem.* **1987**, *91* (19), 5139–5144.
- (32) Ronning, C.; Feldermann, H.; Merk, R.; Hofsass, H.; Reinke, P.; Thiele, J. Carbon nitride deposited using energetic species: A review on XPS studies. *Phys. Rev. B* **1998**, *58* (4), 2207–2215.
- (33) Kim, C.; Jung, J.; Kim, M.; Kang, T.; Ihm, K.; Kim, K.; Kim, B.; Park, J.; Nam, H.; Hwang, K. Low energy electron beam irradiation promoted selective cleavage of surface furoxan. *Langmuir* **2003**, *19* (10), 4504–4508.
- (34) Batich, C.; Donald, D. X-ray photoelectron-spectroscopy of nitroso-compounds: Relative ionicity of the closed and open forms. *J. Am. Chem. Soc.* **1984**, *106* (10), 2758–2761.
- (35) Hueso, J.; Espinos, J.; Caballero, A.; Cotrino, J.; Gonzalez-Elipe, A. XPS investigation of the reaction of carbon with NO, O-2, N-2 and H₂O plasmas. *Carbon* **2007**, *45* (1), 89–96.
- (36) Land, T. A.; Siekhaus, W. J.; Foltz, M. F.; Behrens, R. In *Condensed-Phase Thermal Decomposition of TATB Investigated by Atomic Force Microscopy (AFM) and Simultaneous Thermogravimetric Modulated Beam Mass Spectrometry (STMBMS)*, International Detonation Symposium, Boston, MA, 1993.
- (37) Hacker, N. Investigation of the polymerization of 1,4-dinitrosobenzene by low-temperature infrared and UV absorption-spectroscopy. *Macromolecules* **1993**, *26* (22), 5937–5942.
- (38) Kerber, S.; Bruckner, J.; Wozniak, K.; Seal, S.; Hardcastle, S.; Barr, T. The nature of hydrogen in X-ray photoelectron spectroscopy: General patterns from hydroxides to hydrogen bonding. *J. Vac. Sci. Technol.* **1996**, *14* (3), 1314–1320.
- (39) Haskins, P. J.; Cook, M. D. In *A Modified Criterion for the Prediction of Shock Initiation Threshold for Flyer Plate and Rod Impacts*, International Detonation Symposium, Coeur d'Alene, ID, 2010; pp 1421–1429.
- (40) Dobratz, B. M. *LLNL Explosives Handbook: Properties of Chemical Explosives and Explosive Simulants*; Lawrence Livermore National Laboratory: Livermore, CA, 1981.
- (41) Coleburn, N.; Liddiard, T. Hugoniot equations of state of several unreacted explosives. *J. Chem. Phys.* **1966**, *44* (5), 1929–.
- (42) McQueen, R. G.; Marsh, S. P.; Taylor, J. W.; Fritz, J. N.; Carter, W. J. *High Velocity Impact Phenomena*; Academic Press: New York, 1970.
- (43) Marsh, S. P. *LASL Shock Hugoniot Data*; University California Press: Berkeley, CA, 1980.
- (44) Bundy, F. Pressure-temperature phase-diagram of elemental carbon. *Phys. A* **1989**, *156* (1), 169–178.
- (45) Danilenko, V. Specific features of synthesis of detonation nanodiamonds. *Combust. Explos. Shock Waves* **2005**, *41* (5), 577–588.
- (46) Osswald, S.; Mochalin, V.; Havel, M.; Yushin, G.; Gogotsi, Y. Phonon confinement effects in the Raman spectrum of nanodiamond. *Phys. Rev. B* **2009**, *80* (7), 075419.
- (47) Danilenko, V. Phase diagram of nanocarbon. *Combust. Explos. Shock Waves* **2005**, *41* (4), 460–466.